Design Optimization of an Energy Harvesting Platform for Self-Powered Wireless Devices in Monitoring of AC Power Lines

Alireza Abasian, *Student Member, IEEE*, Ahmadreza Tabesh, *Member, IEEE*, Abolghasem Zeidaabadi Nezhad, *Member, IEEE*, and Nasrin Rezaei-Hosseinabadi, *Member, IEEE*

***Abstract*—This paper presents the design optimization of a magnetic field energy harvesting platform for self-powered ac power line monitoring devices in smart grid applications. The designed platform can be used with any type of vibration-to-electricity energy conversion schemes including piezoelectric, electromagnetic, and electrostatic energy harvesters. The platform includes a cantilever beam with a miniaturized permanent magnet (PM) at the tip that vibrates due to the interaction with the magnetic field of the ac line. The proposed method analytically determines the optimum geometric orientations of the platform as well as the optimum dimensions of PM to maximize the applied magnetic force to the beam. The validity of the design procedure and its assumptions are verified numerically and experimentally using a piezoelectric energy harvesting platform. The numerical and experimental test results confirm the calculated optimum orientation angles and PM dimensions that maximize the magnetic force. The analysis shows that for a PM with vibration direction in a plane normal to the power line, the maximum force can be achieved at the multiples of $+45^\circ$ with reference to the vibration direction. The optimum orientation angle also depends on the angles between the magnetization vector and the direction of the vibration.**

***Index Terms*—Energy harvesting, energy scavenging, magnetic field, monitoring, overhead power lines, self-powered sensor, smart grids, vibration to electricity, wireless sensor.**

I. Introduction

ADVANCES in ultra-low power electronics accelerate the development of self-powered wireless monitoring devices for a wide range of applications including smart grids [1]–[4], structural health monitoring, and biomedical telemetry [5]–[8]. Particularly, smart grids need measuring of overhead ac line quantities (e.g., current, voltage, and temperature) using a widely distributed, reliable, cost-effective, and maintenance-free sensor network [9], [10]. A self-powered wireless sensor, that uses ambient energy for powering its circuitry, is among promising solutions for developing a maintenance-free sensor network in smart grids [11]. This paper deals with magnetic field energy harvesting from overhead ac lines for self-powered monitoring devices.

Energy harvesters are micro-power generators that converter ambient energies into electricity. The main source of energies in a vicinity of an ac line are wind, solar, and ac magnetic field that can be harvested with appropriate devices [12]–[15]. The availability of the magnetic field energy outweighs the alternative resources since the intermittency in wind and solar energies is unavoidable due to weather conditions. The following two schemes have been used for harvesting energy from the magnetic field around an ac power line.

1) A current transformer (CT) based scheme, which uses a magnetic core encircling or sticking on an ac power line [16]–[18]. The bulky structure of this scheme does not allow it to be easily integrated and packaged with a miniaturized wireless sensor device.
2) A cantilever beam with a small magnet at the tip that vibrates at the line frequency [4], [9]. It offers a platform, which can be miniaturized and used with various types of vibration-to-electricity schemes based on cantilever beam such as piezoelectric and magnetic energy harvesters [19], [20].

A CT-based energy harvester offers a higher level of power density (up to 3 mW/cm^3 [16], [21]) that is well-above the required power density for recent ultra-low power wireless sensor nodes. One the other hand, the power density of a vibration-based energy harvester is in the order of 100 μW/cm^3 (up to 800 μW/cm^3 [22], [23]), which is large enough to supply wireless sensor nodes [24]. This paper focuses on the design optimization of the latter scheme. So far, several circuit topologies and numerous techniques are reported for optimizing the captured power from mechanical vibrations [25]–[28]. In all of these works, it is assumed that the vibration source is given and fixed and the main focus is on capturing the maximum kinetic energy of the vibrating beam using the power converter circuit. However, in the case of magnetic field energy harvesting, it is also important to properly select the location and direction of the beam to maximize the vibration force.

This paper demonstrates an analytical design method for the magnetic field energy harvesting platform to maximize the applied force to the device. Then, it determines the optimum

Manuscript received June 9, 2017; revised August 25, 2017 and October 27, 2017; accepted November 13, 2017. Date of publication November 20, 2017; date of current version September 28, 2018. This work was supported in part by Esfahan Regional Electric Company, Isfahan, Iran, under complementary grant for Ph.D. students. Recommended for publication by Associate Editor C. T. Rim. *(Corresponding author: Ahmadreza Tabesh)*

The authors are with the Department of Electrical and Computer Engineering, Isfahan University of Technology, Isfahan 84156-83111, Iran (e-mail: a.tabesh@cc.iut.ac.ir; a.abasian@ec.iut.ac.ir; zeidabad@cc.iut.ac.ir; n.rezaei@cc.iut.ac.ir).

Color versions of one or more of the figures in this paper are available online at http://ieeexplore.ieee.org.

Digital Object Identifier 10.1109/TPEL.2017.2775961

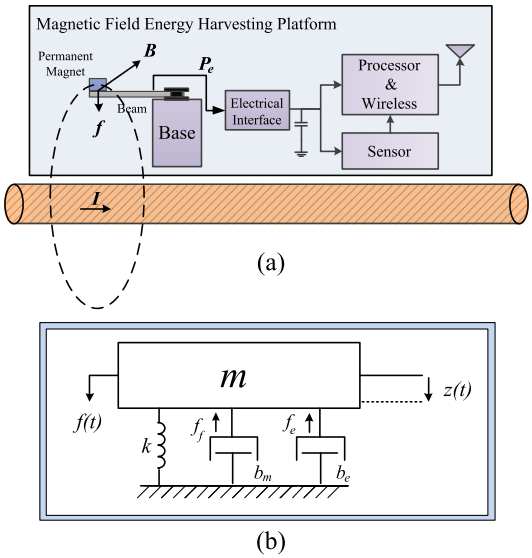

Fig. 1. (a) Schematic of a self-powered wireless monitoring device. (b) Mass-spring-damper representation of the energy harvesting platform.

location and direction of the beam with reference to the direction of an ac power line. The paper also presents a method for optimizing the size of the magnet subjected to the resonance condition of the beam with the power line frequency. The suggested design method is confined to the energy harvesters that use a cantilever beam structure but it is independent of the type of energy harvesters (piezoelectric, electrostatic, and electromagnetic). The validity of the analytical method and its assumptions are verified based on numerical simulations and experimental test results of a prototype system.

II. Architecture and Power Efficiency of a Self-Powered Wireless Monitoring Sensor

A. Self-Powered Wireless Sensor for Grid Monitoring

The block diagram of a power line monitoring device is shown in Fig. 1(a). The main components of this device are sensor, processor, and wireless units. In the case of self-powered devices, these units are supplied with a magnetic field energy harvester, e.g., by using a vibration-to-electricity scheme. In this architecture, the vibration force, f, stems from the interaction between the ac line magnetic field, B, and the permanent magnet at the tip of the beam.

To study the electromechanical behavior of the vibration-to-electricity device, conventionally a mass-spring-damping model with an electric damper is used [22], [29]. Fig. 1(b) shows the block diagram of the model where m, k, and b_m are effective mass, stiffness, and mechanical damping coefficient of the beam, respectively. Also, $z(t)$ denotes the beam tip deflection and f_f represents mechanical frictional force. The parameter b_e represents the effect of an energy harvesting device, which captures a part of the beam vibration energy and converts it to electricity. The parameter b_e is defined such that $f_e = b_e\dot{z}$ is the equivalent electric force applied to the beam with an average power equals to the average of the captured electric power, P_e.

B. Power Efficiency of the Energy Harvesting Platform

The dynamic model of the vibration-to-electricity energy harvesting platform is [22], [29]

$$m\ddot{z} + (b_m + b_e)\dot{z} + kz = f. \tag{1}$$

This model can be represented in the standard form of a second-order system as

$$\ddot{z} + 2(\zeta_m + \zeta_e)\omega_n\dot{z} + \omega_n^2 z = \frac{f}{m} \tag{2}$$

where $\omega_n = \sqrt{k/m}$ is the natural frequency of the beam, $\zeta_m = b_m/(2m\omega_n)$ is the mechanical damping ratio. Similarly, the electrical damping ratio is defined as $\zeta_e = b_e/(2m\omega_n)$. The best performance of the energy harvester can be achieved when the power line frequency matches the resonance frequency of the beam. Assume that the sinusoidal magnetic force is $f(t) = F_m\cos(\omega_n t)$ where F_m is the amplitude of the force. Then, under resonance condition $m\ddot{z} = -kz$ and

$$2(\zeta_m + \zeta_e)\omega_n\dot{z} = \frac{F_m}{m}\cos(\omega_n t). \tag{3}$$

The instantaneous power consumed by the electric load and mechanical friction is $p(t) = (f_f + f_e)\dot{z}$. Therefore, using (1)–(3), the average power, P, under resonance condition can be obtained as

$$P = \frac{1}{T}\int_T (b_m + b_e)\dot{z}^2 dt = \frac{F_m^2}{4m(\zeta_m + \zeta_e)\omega_n} \tag{4}$$

where $T = 2\pi/\omega_n$. Similarly, the average electric power is

$$P_e = \frac{1}{T}\int_T b_e\dot{z}^2 dt = \frac{\zeta_e F_m^2}{4m(\zeta_m + \zeta_e)^2\omega_n}. \tag{5}$$

Based on (5), P_e is proportional to the square of the applied force, F_m^2, and it is also proportional to the device efficiency, defined as $\eta = P_e/P = \zeta_e/(\zeta_e + \zeta_m)$. Thus, maximizing the magnetic force will increase the average electric power. In case using interface circuit with a dc-link energy storage, the electrical damping ζ_e seen by the piezoelectric beam can be adjusted at its optimum value $\zeta_e = \zeta_m$ to maximize the captured power as

$$P_{e_{\max}} = \frac{F_m^2}{16m\zeta_m\omega_n}. \tag{6}$$

Thus, when an interface circuit is used, again based on (6) increasing the magnetic force will increase the average captured electric power.

III. Proposed Method for the Design of the Magnetic Field Energy Harvesting Platform

A. Magnetic Force Calculation

To formulate the applied force to the vibrating platform in Fig. 1(a), the following assumptions and facts are used.

1) It is assumed that the magnetization vector ($\vec{M}$) of the PM is uniform, i.e., $\vec{M} = M_0\hat{u}$ where M_0 is the magnitude of $\vec{M}$ and $\hat{u}$ is the unit vector showing the direction of $\vec{M}$. Therefore, the volume magnetization current density is zero since $\vec{J}_v = \nabla\times\vec{M} = M_0\nabla\times\hat{u} = 0$ and the

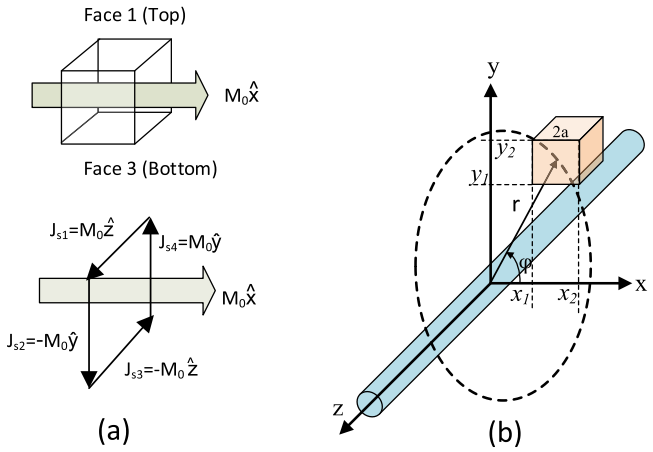

Fig. 2. (a) Representation of PM with surface magnetization current densities. (b) Geometry of PM with reference to an ac power line.

cuboidal PM can be modeled with surface magnetization current density on the cube faces as shown on Fig. 2(a).

2) The magnetization current density corresponding to the face S is $\vec{J}_s = \vec{M} \times \hat{n}$ where $\hat{n}$ is the unit vector normal to S. For a cuboidal PM with $\vec{M}$ along the x-axis [see Fig. 2(a)] the magnetization current density for the top and bottom faces are $\vec{J}_{s1,3} = \pm M_0 \hat{z}$; and for the front and back faces are $\vec{J}_{s2,4} = \mp M_0 \hat{y}$, respectively.
3) It is assumed that the z-axis is aligned with the power line and the direction of vibration is selected along the x-axis as shown in Fig. 2(b). Using this convention, it is proved (Appendix A) that for a PM with $\vec{M} = M_0 \hat{z}$ the resultant magnetic force is zero. Hence, only PMs with magnetization vector in xy-plan are investigated.
4) The power line is assumed to be a single stranded conductor that can be used for transmission lines up to 220 kV. Herein, bundled conductors are excluded from the scope of this analysis. It is also assumed that the weight of PM is negligible compared with the magnetic force due to the magnetic field.

Further, it is assumed that the rare earth permanent magnet (neodymium) is used in the energy harvester. The static demagnetization curve (B-H curve) of a PM is a nonlinear curve. However, in case using rare earth PMs, this curve can be estimated with a linear function since the coercive force for this type of magnets is significantly high compared with other permanent magnets such as Alnico [30].

Using the Lorentz force and Biot–Savart law formulations [31], the applied force to PM due to the ac line current can be obtained from the surface integral over the magnetization current densities (J_{s1} to J_{s4}) at the top, front, bottom, and back surfaces of PM shown on Fig. 2(a), as

$$\vec{F}_m^x = \sum_{l=1}^{4} F_l^x \cdot \hat{x} = \sum_{k=1}^{4} \left(\int_{S_k} \vec{J}_{s_k} \times \left(\frac{\mu_0 I_m}{2\pi r} \hat{\phi} \right) dS \right) \cdot \hat{x} \quad (7)$$

where F_m^x is the amplitude of the applied force to a PM with $\vec{M} = M_0 \hat{x}$ along the x-axis; F_l^x is the applied force corresponding to face l, and superscript ^{x} denotes that the force is calculated for a PM with magnetization vector along x-axis. Also, I_m, r, ϕ, and μ_0 denote the amplitude of power line current; the radial distance between the center of PM cube and the axis of the power line; the azimuth unit vector; and the permeability of free space, respectively.

The radial distances for the faces 2 and 4 are the same and these two faces correspond to the current density vectors with opposite directions. Thus, $\vec{F}_2^x + \vec{F}_4^x = 0$ and based on (7), F_1^x and F_3^x are

$$\begin{aligned} \vec{F}_1^x &= \frac{\mu_0 M_0 I_m}{2\pi} \int_{S_{1_{(y=y_2)}}} \hat{z} \times \frac{1}{r} \hat{\phi} dx dz \\ &= \frac{\mu_0 M_0 I_m z_c}{-\pi} \int_{x_1}^{x_2} \hat{z} \times \frac{1}{r} \hat{\phi} dx \end{aligned} \quad (8)$$

$$\begin{aligned} \vec{F}_3^x &= \frac{\mu_0 M_0 I_m}{-2\pi} \int_{S_{3_{(y=y_1)}}} \hat{z} \times \frac{1}{r} \hat{\phi} dx dz \\ &= \frac{\mu_0 M_0 I_m z_c}{-\pi} \int_{x_1}^{x_2} \hat{z} \times \frac{1}{r} \hat{\phi} dx \end{aligned} \quad (9)$$

where PM dimensions are $2x_c \times 2y_c \times 2z_c$ and

$$\hat{z} \times \frac{1}{r} \hat{\phi} = \frac{x}{x^2 + y^2} \hat{x} + \frac{y}{x^2 + y^2} \hat{y} \quad (10)$$

$$\int \hat{z} \times \frac{1}{r} \hat{\phi} dx = \frac{1}{2} \ln(x^2 + y^2) \hat{x} + \tan^{-1} \left(\frac{x}{y} \right) \hat{y}. \quad (11)$$

Substituting for $\hat{z} \times \hat{\phi}/r$ from (10) in (8) and evaluating the integral at $y = y_1$ for the face 3 and $y = y_2$ for the face 1, we obtain

$$\vec{F}_m^x = \vec{F}_{1_x}^x + \vec{F}_{3_x}^x = \frac{\mu_0 M_0 I_m z_c}{2\pi} \left(\ln \frac{(x_2^2 + y_1^2)(x_1^2 + y_2^2)}{(x_2^2 + y_2^2)(x_1^2 + y_1^2)} \right) \quad (12)$$

where $F_{1_x}^x$ and $F_{2_x}^x$ are the x-axis components of F_1^x and F_2^x, respectively. Similar procedure can be adopted to obtain the magnetic force for a PM with magnetization vector aligned with y-axis, i.e., $\vec{F}_m^y$ with $\vec{M} = M_0 \hat{y}$. Thus, $\vec{F}_m^y$ can be readily obtained by rotating the xy-axes by 90°, that yields

$$\vec{F}_m^y = \frac{\mu_0 M_0 I_m z_c}{\pi} \sum_{i=1}^{2} \sum_{j=1}^{2} (-1)^{i+j} \left(\tan^{-1} \left(\frac{y_i}{x_j} \right) \right). \quad (13)$$

B. Optimizing the Platform Location

To maximize the applied magnetic force to a platform with respect to the location (orientation) of the beam, the magnetic forces F_m^x and F_m^y in (12) and (13) are investigated at various positions around the power line. To find the best orientation for PM location, x and y coordinations of the center of PM are substituted in terms of r and ϕ as

$$\begin{aligned} x_1 &= -x_c + r\cos\phi, \quad & x_2 &= x_c + r\cos\phi \\ y_1 &= -y_c + r\sin\phi, \quad & y_2 &= y_c + r\sin\phi \end{aligned} \quad (14)$$

where r is the radial distance between the center of the PM and the axis of the power line (z-axis), and ϕ is the angle of $\vec{r}$ with reference to x-axis. Assuming $x_c = y_c = a$ in (14) and

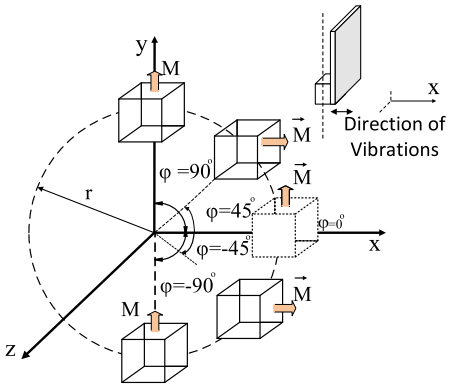

Fig. 3. Optimum orientations of the platform for PMs with x- and y-axis magnetization vectors.

substituting for x_1, y_1, x_2, and y_2 in (12) yields

$$F_m^x = \frac{\mu_0 M_0 I_m z_c}{2\pi}\left[\ln\frac{(a+r\cos\phi)^2+(-a+r\sin\phi)^2}{(a+r\cos\phi)^2+(a+r\sin\phi)^2} + \ln\frac{(-a+r\cos\phi)^2+(a+r\sin\phi)^2}{(-a+r\cos\phi)^2+(-a+r\sin\phi)^2}\right]. \tag{15}$$

Simplifying and rearranging (15) (Appendix B), we deduce

$$F_m^x = \frac{\mu_0 M_0 I_m z_c}{2\pi}\ln\left(\frac{H_a+\sin 2\phi}{H_a-\sin 2\phi}\right) \tag{16}$$

where $H_a = (2a^2+r^2)^2/(4a^2r^2) - 1$. Thus, the optimum location of PM with respect to ϕ can be obtained as

$$\frac{dF_m^x}{d\phi} = \frac{2\mu_0 M_0 H_a I_m z_c \cos(2\phi)}{\pi(H_a^2-\sin^2(2\phi))} = 0 \Rightarrow \phi = (2k+1)\frac{\pi}{4} \tag{17}$$

where k is an integer. Similarly, by substituting for PM coordinates from (14) in (13) and simplifying F_m^y (Appendix B), we obtain

$$F_m^y = -\frac{\mu_0 M_0 I_m z_c}{\pi}\tan^{-1}(G_a\cos 2\phi) \tag{18}$$

where $G_a = (2ar)^2/(r^4-4a^4)$ and the optimum orientation of PM can be obtained as

$$\frac{dF_m^y}{d\phi} = \frac{2\mu_0 M_0 G_a I_m z_c \sin(2\phi)}{\pi(1+G_a^2\cos(2\phi)^2)} = 0 \Rightarrow \ \phi = \frac{k\pi}{2}. \tag{19}$$

Thus, the analytical investigation of the magnetic force for $-\pi/2 \le \phi \le \pi/2$ shows that the optimum orientations of a vibrating platform aligned with x-axis are $\phi = \pm\pi/4$ and $\phi = 0, \pm\pi/2$ corresponding to PMs with x- and y-axis magnetization vectors (see Fig. 3).

C. Selection of Permanent Magnet Dimensions

In the design procedure of the platform, the mass and volume of PM are fixed and obtained based on the resonance frequency of the beam. Thus, the selection of PM dimensions can be obtained from the solution of the following constrained optimization problem:

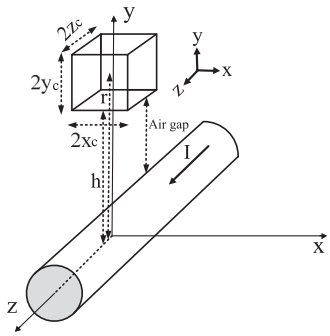

Fig. 4. Schematic of PM with y-axis magnetization and constant h for the dimensions optimization problem.

$$\begin{aligned} &\text{max.} && F_m^{x,y}(x_c, y_c, z_c) \\ &\text{subject to} && (2x_c)(2y_c)(2z_c) = V_{\text{PM}} \end{aligned} \tag{20}$$

where V_{PM} is the volume of PM. This optimization problem can be solved using numerical and/or analytical methods such as the Lagrange multipliers method. In special cases, however, a simpler method can be adopted as shown in Fig. 4 for a PM with y-axis magnetization vector that is located at its optimum orientation $\phi = \pi/2$. In this case, r is not constant and rather we assume the distance between z-axis and the edge of PM, h, is constant. Practically, h is the least distance between the axis of the line and the edge of the platform that is determined by the mechanical and installation constraints. Substituting for $x_1 = -x_c$, $x_2 = x_c$, $y_1 = h$, and $y_2 = h + 2y_c$ in (13), we deduce

$$\vec{F}_m^y = \frac{2\mu_0 M_0 I_m z_c}{\pi}\left(\tan^{-1}\left(\frac{h+2y_c}{x_c}\right) - \tan^{-1}\left(\frac{h}{x_c}\right)\right) \tag{21}$$

that can be rearranged to

$$\vec{F}_m^y = \frac{2\mu_0 M_0 I_m z_c}{\pi}\tan^{-1}\left(\frac{2x_c y_c}{h^2+2hy_c+x_c^2}\right). \tag{22}$$

Assuming that $2z_c$ is selected based on mechanical constraints, e.g., $2z_c = W$ where W is the width of the vibrating beam. Then, considering $y_c = V_{\text{PM}}/(4Wx_c)$, the force can be expressed in terms of x_c as

$$\vec{F}_m^y = \frac{\mu_0 W M_0 I_m}{\pi}\tan^{-1}\left(\frac{2V_{\text{PM}}x_c}{4Wx_c^3+4Wh^2x_c+2hV_{\text{PM}}}\right). \tag{23}$$

Finding the zeros of the first derivative of (23) yields the maximum of F_m^y for $2z_c = W$ and

$$2x_c = 2\sqrt[3]{V_{\text{PM}}h/(4W)}, \quad 2y_c = 0.5\sqrt[3]{4V_{\text{PM}}^2/(hW^2)}. \tag{24}$$

IV. Verification of the Design Method

A. Test Setup and Description of the Test Method

The validity of the analytical design optimization method is investigated based on comparing the analytical results with the numerical and experimental results using a test setup. Fig. 5(a) shows the schematic of the test setup that includes an autotransformer connected to a 0.4 kVA, 220/6 V isolating transformer.

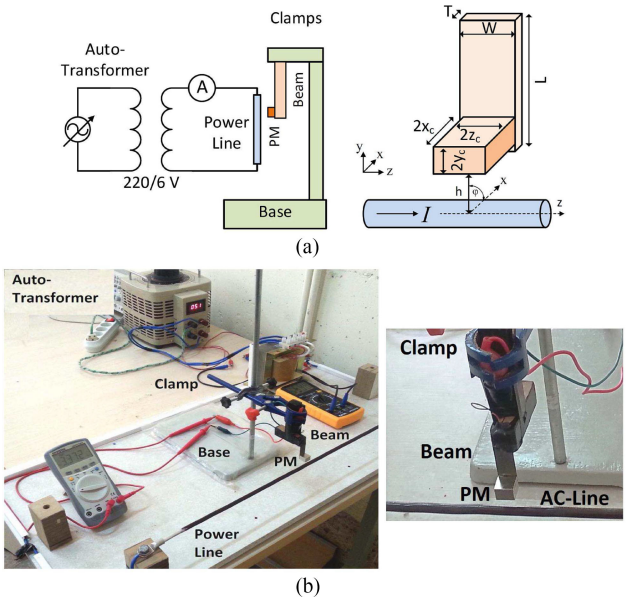

Fig. 5. (a) Block diagram of the test setup and the vibrating beam in magnetic energy harvesting platform. (b) Photo of the test setup.

The secondary coil of the transformer is shorted with a segment of an ac power line connected to a current meter where the short circuit current can be adjusted by autotransformer at the primary. A clamped PM and vibrating beam that is installed on a base is also located near the line with adjustable angle with respect to the line. Fig. 5(b) shows the photo of the test setup.

The numerical analysis results are produced based on three-dimensional finite analysis (3-D finite element method) of the set up. The numerical analysis includes verifying the optimum locations with respect to the orientation of PM magnetization vectors; and the effect of PM with a constant volume and various dimensions on the applied magnetic force. In the experiment, a piezoelectric beam is used as an energy harvesting device to verify the optimum locations based on the level of open circuit voltage. The parameters of the test setup are listed in Table I.

TABLE I
PARAMETERS OF THE TEST SETUP AND ENERGY HARVESTER

Parameter	Description
Power Line and Setup:	
AC line Diameter	7 mm
AC line Current	11 A (rms)
Frequency	50 Hz
Air gap	4.5 mm
h	8 mm
Permanent Magnets [32]:	
PM Types	NdFeB,
Max. energy	42 MGOe
PM size (mm^3)	$12.7 \times 12.7 \times 0.794$
PM mass	0.96 gr
Number of PMs	12
Piezoelectric Parameters [33]:	
Model	Q220-A4-303YB
Dimensions (mm^3)	$28.6 \times 12.7 \times 0.508$
Resonant frequency (f_r)	250 Hz
Beam effective Mass	0.308 gr
Beam etiffness	$K = 760$ N/m
Beam electromechanical Coupling	$\theta = 1.697$ mN/V
Beam capacitance	$C_p = 55$ nF
Beam electrical coupling	$k_{el} = 0.264$
Damping ratio	$\zeta_m = 0.37$

B. Results and Discussions

In the first study, the analytical model of the applied magnetic force and its assumptions are numerically verified using the finite element analysis. In this study, the applied magnetic force to the PM is calculated at orientation angles span from $-45°$ to $+135°$ with reference to x-axis and for a 1 cm^3 cuboidal PM with the magnetization vectors along x- and y-axis.

Fig. 6(a) shows the analytical force against the numerically calculated force for a PM with magnetization along x-axis with 50 A ac-line current. The diameter of ac-line is 2 cm and air gap distance selected as 3 mm. In this scenario, the maximum force is 31.129 mN that occurs at orientation angles at $-45°$, $+45°$, and $+135°$. As expected, the numerical analysis also shows that the maximum force occurs at $(2k+1)\pi/4$ orientation angles. To investigate the matching between the analytical and numerical results, the correlation coefficient R is used. This coefficient is

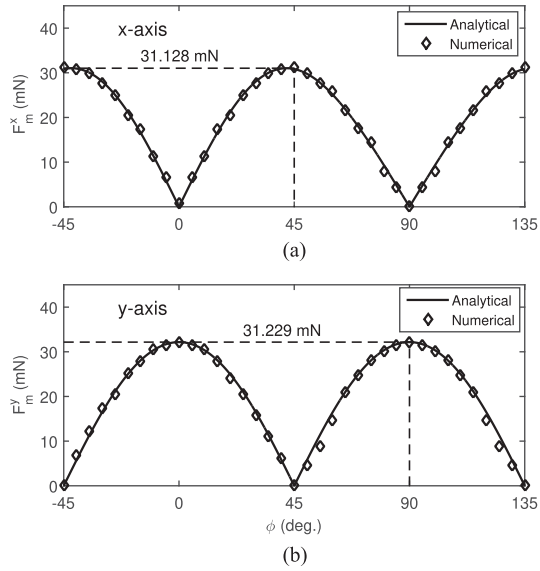

Fig. 6. Analytical and finite element numerical calculation results for amplitudes of the magnetic forces with respect to the orientation angles for a PM with: (a) x-axis; and (b) y-axis magnetization vectors.

a statical measure for the goodness of fit that is defined as

$$R = \sqrt{\left(1 - \sum_i (y_i - f_i)^2 / \sum_i (y_i - \bar{y})^2\right)} \qquad (25)$$

where $[y_1\ y_2 \cdots y_n]^T$ is the measured vector and $[f_1\ f_2 \cdots f_n]^T$ is the vector of predicted value based on a model, and $\bar{y} = \sum_{i=1}^{n} y_i$ is the average of the measured values. R is between 0 to 1 (or 100%) and for a perfect fit, $R = 1$. In Fig. 6(a), the numerical results are fitted with those obtained from the analytical model with correlation coefficient $R = 0.9984$ that shows a close match between the analytical and numerical results.

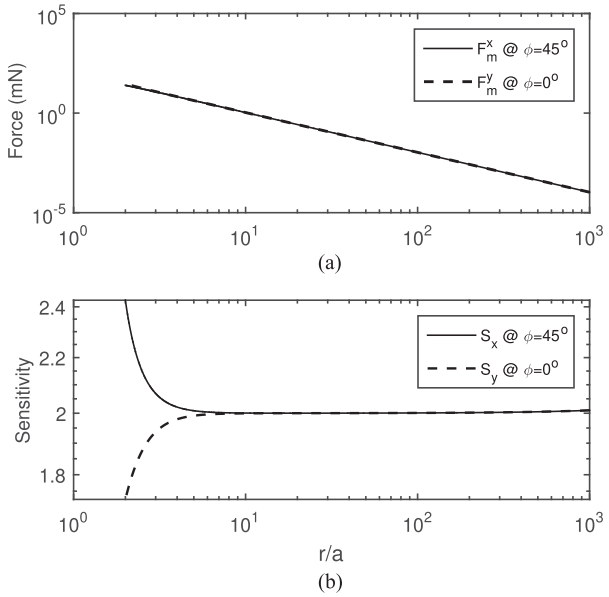

Fig. 7. (a) Variations of the applied forces with respect to distance from the power line. (b) Sensitivity of the forces.

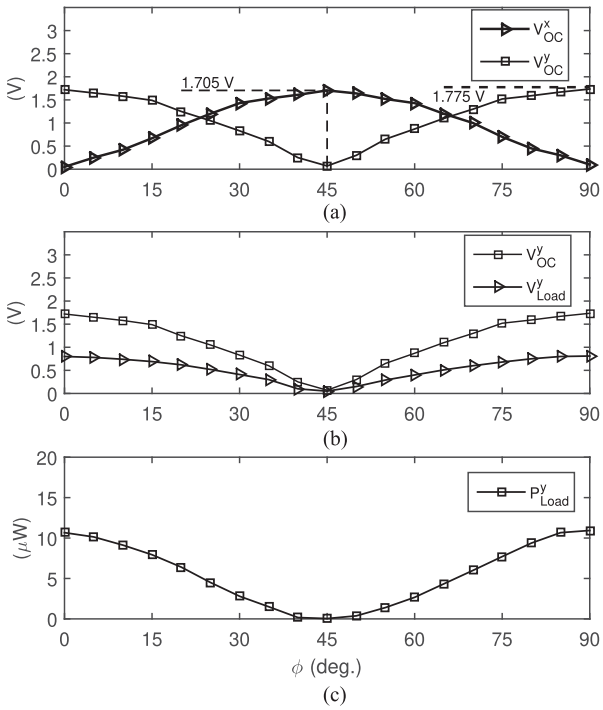

Fig. 8. (a) Measured open circuit voltage for the PMs with magnetization vectors along x and y axes ($V^x_{\rm OC}$ and $V^y_{\rm OC}$). (b) Comparison of $V^y_{\rm OC}$ with the measured voltage across the resistive load $R_L = 60\,\text{k}\Omega$. (c) Calculated electric power for $R_L = 60\,\text{k}\Omega$.

Fig. 6(b) also shows the magnetic forces for a PM with y-axis magnetization vector which is vibrating in x-axis direction. The study results demonstrate a close match between the analytical model and numerical results with the correlation coefficient $R = 0.9974$. Further, the numerical results also verify that the maximum force 31.229 mN occurs at 0° and +90°, which are predicted based on the analytical model. There is a slight difference between the maximum force for PMs with magnetization vectors in x and y directions [see Fig. 5(a) and (b)]. It can be justified due to cuboidal shape of PM that leads asymmetry in geometry for the orientations along $\phi = \pm 45^\circ$ and $\phi = 0$ (or $\phi = 90^\circ$).

Fig. 7(a) shows that the applied forces to both PMs with x- and y-axis significantly decrease as the distance of PMs from the power line is increased. This recommends that PM should be installed as close as possible to a power line for maximizing the force. Further, it verifies that for an energy harvester installed on one power line, the effect of other power lines is negligible. The reason is that the magnet dimension (a) is practically less than 1 cm while the distance between the lines is several tens of centimeters and therefore $r/a \gg 10$. Fig. 7(b) shows the sensitivity of the forces F^x_m at $\phi = 45^\circ$ and F^y_m at $\phi = 0^\circ$ with respect to r/a ratio. The S_x and S_y functions are defined as

$$S_x = \left(\frac{(r/a)}{F^x_m}\right)\frac{\partial F^x_m}{\partial (r/a)},\quad S_y = \left(\frac{(r/a)}{F^y_m}\right)\frac{\partial F^y_m}{\partial (r/a)}. \tag{26}$$

The graphs of S_x and S_y show that the forces are sensitive to distance from a power line especially for $r/a < 10$. Hence, the energy harvester installed in a vicinity of one power line is less sensitive to the magnetic field of other power lines in a three-phase system.

For piezoelectric energy harvesters, the amplitude of vibration (U) is proportional to the open circuit voltage as $U = C_p V_{\rm oc}/\theta$ where C_p, $V_{\rm OC}$ and θ are the capacitance, open circuit voltage, and electromechanical coupling of the piezoelectric beam [29], [34], [35]. Further, the amplitude of vibration is a function of applied force to the beam. Thus, the relationship between the force and voltage can be expressed as [34], [35]

$$F_m = \frac{V_{\rm OC} M C_p}{\theta}\sqrt{\left(\frac{K}{M}(1+k^2_{el}) - \omega^2\right)^2 + 4\frac{K}{M}\zeta^2_m\omega^2} \tag{27}$$

where k_{el} and C_p denote the electrical coupling and capacitance of the beam, respectively. Fig. 8(a) shows the measured voltages at various orientation angles span from 0° to +90° with respect to the x-axis and for PMs with magnetization vectors along x- and y-axes. As Fig. 8(a) shows for PM with x-axis magnetization vector the maximum voltage of $V^x_{\rm OC} = 1.705$ V occurs at +45° and for PM with y-axis two maximum points of $V^y_{\rm OC}$ occur at 0° and +90°. The optimum orientation angles in this experiment confirm the results obtained from the analytical and numerical analyses. Furthermore, consistent with the previous analytical and numerical results in Fig. 6(a) and (b), the experiment test results also show that the peak values of V^y_m at 0° and 90° are slightly greater than the peak of V^x_m at +45°.

Fig. 8(b) and (c) show the voltage and electric power of the piezoelectric energy harvester when it is connected to a resistive load, R_L. The resistive load is selected $R_L = 60\,\text{k}\Omega$ to be matched with capacitive impedance of the piezoelectric beam (i.e., $R_L = 1/(C_p\omega)$) for capturing the maximum electric power. Fig. 8(b) and (c) confirm that under load condition again the maximum voltage and power occur at $\phi = 0$ and $\phi = 90^\circ$.

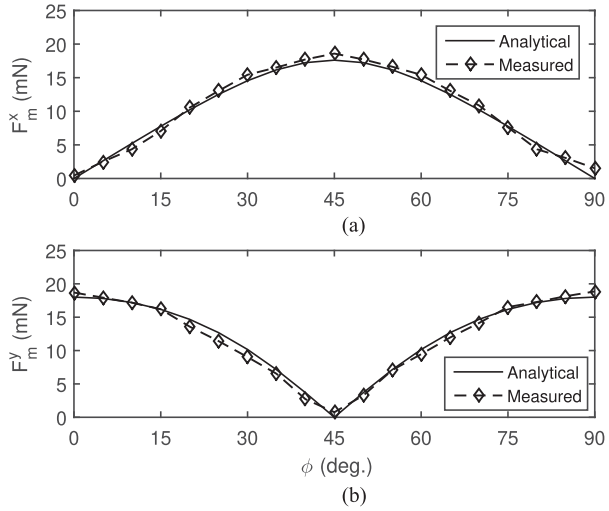

Fig. 9. Calculated forces based on measured open circuit voltages $V^x_{\rm OC}$ and $V^y_{\rm OC}$ for the PMs with. (a) x-axis. (b) y-axis magnetization vectors.

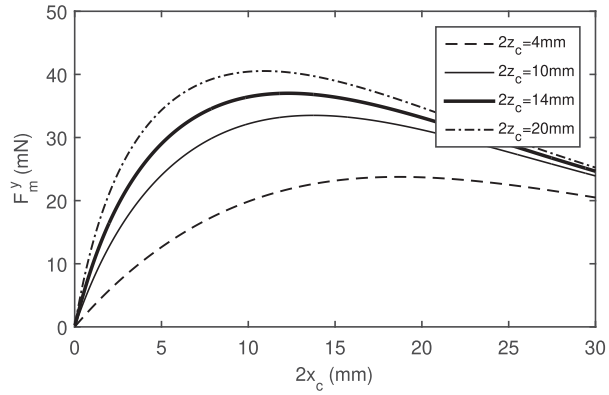

Fig. 10. Amplitude of magnetic force for a PM with constant volume and various dimensions.

Using (27) with the piezoelectric beam parameters as listed in Table I, the applied force can be obtained as shown in Fig. 9(a) and (b). Comparing the calculated forces based on measured voltages with the forces obtained from the analytical model shows a close match with correlation coefficient $R = 0.9987$ for the x-axis and $R = 0.9982$ for the y-axis magnetization vectors, respectively.

To investigate the effect of PM dimensions on the applied force, PM with magnetization direction along y-axis is considered. It is assumed that the volume of the PM is fixed at 1 cm^3 and the applied force for different width are calculated. Fig. 10 shows the variation of force with respect to $2x_c$ dimension for different width $2z_c$ = 4, 10, 14, and 20 mm based on (23). The curves in Fig. 10 show that for each width there exits an optimum dimension that is analytically given by (24). Further, the analytical results show that increasing the width of PM ($2z_c$) increases the maximum force. Therefore, to maximize the force, first the width of PM, $2z_c$, is selected at its maximum value that can be defined with mechanical packaging constrains, e.g., the width of the beam. Then, for the selected $2z_c$, the $2x_c$, and $2y_c$ dimensions are obtained based on (24) to obtain the maximum force.

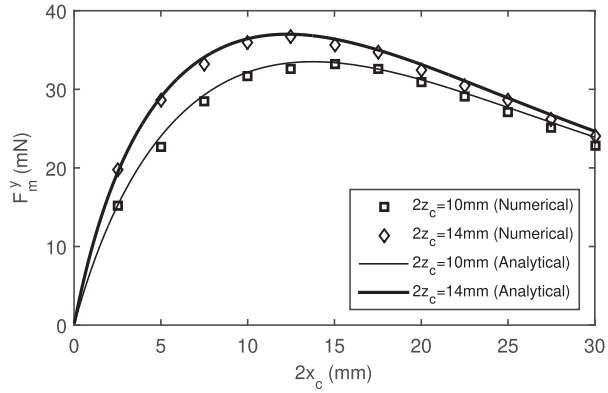

Fig. 11. Numerical results and analytically calculated magnetic forces for a PM with fixed volume at various dimensions.

To verify the validity of the model in (23) and the optimum dimensions in (24), the magnetic forces for various $2x_c$ are numerically calculated and compared with the analytical results based on (23). Fig. 11 shows the numerical results against the analytical ones for $2z_c = 10$ and 14 mm. The correlation coefficients for $2z_c = 10$ and 14 mm are $R = 0.9985$ and $R = 0.9984$, respectively, which show a close match between numerical and analytical results.

V. Conclusion

A design optimization procedure for magnetic energy harvesting platforms is presented in this paper that is useful for deployment of self-powered wireless sensor nodes for monitoring of ac line parameters. The design method determines the optimum orientation angle of a PM with respect to the direction of the vibration for various PM magnetization vectors. Furthermore, the method presents an analytical formulation to obtain the optimum dimensions for PM to maximize the magnetic force. The suggested method can be used for any type of energy harvesting device and the validity of the analytical formulations and models are verified based on numerical analysis of a test system. The test results for optimum orientation angles are also experimentally verified using a piezoelectric energy harvester beam, which is installed in a vicinity of an ac power line.

Appendix A
Magnetic Force for PM With z-axis Magnetization

Assume that the PM in Fig. 2 is a cube with $2a$ edges and $\vec{M} = M_0\hat{z}$. Then, the force component due to PM cube face at $y = y_2$ is

$$\vec{F_1} = \int_{S_{(y=y_1)}} -M_0\hat{x} \times \frac{\mu_0 I_m}{2\pi r}\hat{\phi}dxdz. \tag{28}$$

Substituting $r = \sqrt{x^2 + y^2}$ and $\hat{\phi} = -\sin\phi\hat{x} + \cos\phi\hat{y}$ in (28) yields

$$\vec{F_1} = -\frac{\mu_0 M_0 I_m a}{\pi}\int_{x_1}^{x_2} \frac{\cos\phi}{r}\hat{z}dx = \tag{29}$$

and since $\cos\phi = x/\sqrt{x^2+y^2}$, we obtain

$$\vec{F}_1 = -\frac{\mu_0 M_0 I_m a}{2\pi} \ln \frac{x_2^2+y_2^2}{x_1^2+y_2^2}\hat{z}. \tag{30}$$

Similarly, the force component corresponding to the cube face at $y = y_1$ and with magnetization current density in opposite the cube face at $y = y_2$, is

$$\vec{F}_3 = \frac{\mu_0 M_0 I_m a}{2\pi} \ln \frac{x_2^2+y_1^2}{x_1^2+y_1^2}\hat{z}. \tag{31}$$

For the cube face at $x = x_1$ the magnetic force component is

$$\vec{F}_2 = \int_{S_{(x=x_1)}} -M_0\hat{y} \times \frac{\mu_0 I_m}{2\pi r}\hat{\phi} dydz. \tag{32}$$

Thus,

$$\vec{F}_2 = -\frac{\mu_0 M_0 I_m a}{\pi} \int_{y_1}^{y_2} \frac{\sin\phi}{r}\hat{z} dy \tag{33}$$

and we obtain

$$\vec{F}_2 = -\frac{\mu_0 M_0 I_m a}{2\pi} \ln(x^2+y^2)\hat{z}. \tag{34}$$

Similarly, for the cube face at $x = x_2$ the force component is

$$\vec{F}_4 = \frac{\mu_0 M_0 I_m a}{2\pi} \ln \frac{x_2^2+y_2^2}{x_2^2+y_1^2}\hat{z}. \tag{35}$$

Thus, the total force for a PM with $\vec{M} = M_0\hat{z}$ is

$$\vec{F}_m^z = \sum_{k=1}^{4} \vec{F}_k = \frac{\mu_0 M_0 I_m a}{-2\pi} \ln \left(\frac{\left(\frac{x_2^2+y_2^2}{x_1^2+y_2^2}\right)\left(\frac{x_1^2+y_2^2}{x_1^2+y_1^2}\right)}{\left(\frac{x_2^2+y_1^2}{x_1^2+y_1^2}\right)\left(\frac{x_2^2+y_2^2}{x_2^2+y_1^2}\right)} \right)\hat{z} \tag{36}$$

that can be simplified to

$$\vec{F}_m^z = -\frac{\mu_0 M_0 I_m a}{2\pi} \ln(1)\hat{z} = 0. \tag{37}$$

Thus, (37) concludes that the magnetic force for a PM with magnetization vector in parallel with the line current is zero.

APPENDIX B
DETAILS OF F_m^x AND F_m^y

To obtain (16), first we define $K_x \triangleq (\mu_0 M_0 I_m z_c)/(2\pi)$ and start with (15)

$$F_m^x = K_x \left[\ln \frac{2a^2+r^2+2ar(\cos\phi-\sin\phi)}{2a^2+r^2+2ar(\cos\phi+\sin\phi)} + \ln \frac{2a^2+r^2-2ar(\cos\phi-\sin\phi)}{2a^2+r^2-2ar(\cos\phi+\sin\phi)} \right] \tag{38}$$

that can be simplified as

$$F_m^x = K_x \left[\ln \frac{(2a^2+r^2)^2-4a^2r^2(\cos\phi-\sin\phi)^2}{(2a^2+r^2)^2-4a^2r^2(\cos\phi+\sin\phi)^2} \right] \tag{39}$$

and

$$F_m^x = K_x \left[\ln \frac{\left(\frac{(2a^2+r^2)}{2ar}\right)^2-(1-\sin 2\phi)}{\left(\frac{(2a^2+r^2)}{2ar}\right)^2-(1+\sin 2\phi)} \right]. \tag{40}$$

Finally, (40) can be simplified into

$$F_m^x = K_x \ln \frac{H_a+\sin 2\phi}{H_a-\sin 2\phi} \tag{41}$$

where $H_a = (2a^2+r^2)^2/(2ar)^2 - 1$. To obtain (18), the identity

$$\tan^{-1}\alpha + \tan^{-1}\beta = \tan^{-1}\left(\frac{\alpha+\beta}{1-\alpha\beta}\right). \tag{42}$$

is used for the simplification of

$$F_m^y = K_x \sum_{i=1}^{2}\sum_{j=1}^{2} \left(\tan^{-1}\left(\frac{y_i}{x_j}\right)\right)(-1)^{i+j} \tag{43}$$

that yields

$$F_m^y = K_x \left(\tan^{-1}\frac{x_2(y_2-y_1)}{x_2^2+y_2y_1}) + \tan^{-1}\frac{x_1(y_1-y_2)}{x_1^2+y_2y_1} \right) \tag{44}$$

and it can be also simplified as

$$F_m^y = K_x \tan^{-1}\frac{y_2y_1-x_2x_1}{\Delta} \tag{45}$$

where

$$\Delta = \frac{(x_2x_1+y_2y_1)^2}{(x_2-x_1)(y_2-y_1)} + y_1y_2\frac{x_2-x_1}{y_2-y_1} + x_1x_2\frac{y_2-y_1}{x_2-x_1}.$$

Substituting $x_2 = x_1 + 2a$ and $y_2 = y_1 + 2a$ in (45), we obtain

$$F_m^y = K_x \tan^{-1}\left[\frac{4a^2(y_2y_1-x_2x_1)}{(x_2x_1+y_2y_1)^2+4a^2(x_2x_1+y_2y_1)}\right]. \tag{46}$$

Finally, by substituting $y_2y_1 - x_2x_1 = -r^2\cos 2\phi$ and $y_2y_1 + x_2x_1 = r^2 - 2a^2$, we obtain

$$\vec{F}_m^y = -K_x \tan^{-1}(G_a\cos 2\phi) \tag{47}$$

where $G_a = (2ar)^2/(r^4-4a^4)$.

REFERENCES

[1] A. Khaligh, P. Zeng, and C. Zheng, "Kinetic energy harvesting using piezoelectric and electromagnetic technologies, state of the art," *IEEE Trans. Ind. Electron.*, vol. 57, no. 3, pp. 850–860, Mar. 2010.

[2] J. Han, J. Hu, Y. Yang, Z. Wang, S. X. Wang, and J. He, "A nonintrusive power supply design for self-powered sensor networks in the smart grid by scavenging energy from ac power line," *IEEE Trans. Ind. Electron.*, vol. 62, no. 7, pp. 4398–4407, Jul. 2015.

[3] M. Erol-Kantarci and H. T. Mouftah, "Wireless sensor networks for cost-efficient residential energy management in the smart grid," *IEEE Trans. Smart Grid*, vol. 2, no. 2, pp. 314–325, Jun. 2011.

[4] B. Fateh, M. Govindarasu, and V. Ajjarapu, "Wireless network design for transmission line monitoring in smart grid," *IEEE Trans. Smart Grid*, vol. 4, no. 2, pp. 1076–1086, Jun. 2013.

[5] B. Martinez, X. Vilajosana, F. Chraim, I. Vilajosana, and K. S. Pister, "When scavengers meet industrial wireless," *IEEE Trans. Ind. Electron.*, vol. 62, no. 5, pp. 2994–3003, May 2015.

[6] J. L. Wardlaw, I. Karaman, and A. I. Karsilayan, "Low-power circuits and energy harvesting for structural health monitoring of bridges," *IEEE Sens. J.*, vol. 13, no. 2, pp. 709–722, Feb 2013.

[7] Y. Hu *et al.*, "A self-powered system for large-scale strain sensing by combining CMOS ICS with large-area electronics," *IEEE J. Solid-State Circuits*, vol. 49, no. 4, pp. 838–850, Apr. 2014.

[8] L. Zhou, A. C. Abraham, S. Y. Tang, and S. Chakrabartty, "A 5 nw quasi-linear cmos hot-electron injector for self-powered monitoring of biomechanical strain variations," *IEEE Trans. Biomed. Circuits Syst.*, vol. 10, no. 6, pp. 1143–1151, Dec. 2016.

[9] V. C. Gungor, B. Lu, and G. P. Hancke, "Opportunities and challenges of wireless sensor networks in smart grid," *IEEE Trans. Ind. Electron.*, vol. 57, no. 10, pp. 3557–3564, Oct. 2010.
[10] T. Hosseinimehr and A. Tabesh, "Magnetic field energy harvesting from ac lines for powering wireless sensor nodes in smart grids," *IEEE Trans. Ind. Electron.*, vol. 63, no. 8, pp. 4947–4954, Aug. 2016.
[11] D. Briand, E. Yeatman, and S. Roundy, Eds., *Micro Energy Harvesting*. Hoboken, NJ, USA: Wiley, 2015.
[12] O. Cetinkaya and O. B. Akan, "Electric-field energy harvesting in wireless networks," *IEEE Wireless Commun.*, vol. 24, no. 2, pp. 34–41, Apr. 2017.
[13] H. Kim, S. Kim, C. K. Kwon, Y. J. Min, C. Kim, and S. W. Kim, "An energy-efficient fast maximum power point tracking circuit in an 800-uw photovoltaic energy harvester," *IEEE Trans. Power Electron.*, vol. 28, no. 6, pp. 2927–2935, Jun. 2013.
[14] N. Rezaei-Hosseinabadi, A. Tabesh, and R. Dehghani, "A topology and design optimization method for wideband piezoelectric wind energy harvesters," *IEEE Trans. Ind. Electron.*, vol. 63, no. 4, pp. 2165–2173, Apr. 2016.
[15] N. M. Roscoe and M. D. Judd, "Harvesting energy from magnetic fields to power condition monitoring sensors," *IEEE Sens. J.*, vol. 13, no. 6, pp. 2263–2270, Jun. 2013.
[16] R. Moghe, A. R. Iyer, F. C. Lambert, and D. Divan, "A low-cost electric field energy harvester for an mv/hv asset-monitoring smart sensor," *IEEE Trans. Ind. Appl.*, vol. 51, no. 2, pp. 1828–1836, Mar./Apr. 2015.
[17] J. Moon and S. B. Leeb, "Analysis model for magnetic energy harvesters," *IEEE Trans. Power Electron.*, vol. 30, no. 8, pp. 4302–4311, Aug. 2015.
[18] S. Yuan, Y. Huang, J. Zhou, Q. Xu, C. Song, and G. Yuan, "A high-efficiency helical core for magnetic field energy harvesting," *IEEE Trans. Power Electron.*, vol. 32, no. 7, pp. 5365–5376, Jul. 2017.
[19] Q. Zhang and E. S. Kim, "Microfabricated electromagnetic energy harvesters with magnet and coil arrays suspended by silicon springs," *IEEE Sens. J.*, vol. 16, no. 3, pp. 634–641, Feb. 2016.
[20] E. E. Aktakka and K. Najafi, "A micro inertial energy harvesting platform with self-supplied power management circuit for autonomous wireless sensor nodes," *IEEE J. Solid-State Circuits*, vol. 49, no. 9, pp. 2017–2029, Sep. 2014.
[21] S. D. Moss, O. R. Payne, G. A. Hart, and C. Ung, "Scaling and power density metrics of electromagnetic vibration energy harvesting devices," *Smart Mater. Struct.*, vol. 24, no. 2, 2015, Art. no. 023001.
[22] P. D. Mitcheson, T. C. Green, E. M. Yeatman, and A. S. Holmes, "Architectures for vibration-driven micropower generators," *J. Microelectromech. Syst.*, vol. 13, no. 3, pp. 429–440, 2004.
[23] S. Roundy, P. Wright, and J. Rabaey, *Energy Scavenging for Wireless Sensor Networks: With Special Focus on Vibrations.* Norwell, Massachusetts: Kluwer Academic Publishers, 2004.
[24] J. Ayers, K. Mayaram, and T. S. Fiez, "An ultralow-power receiver for wireless sensor networks," *IEEE J. Solid-State Circuits*, vol. 45, no. 9, pp. 1759–1769, Sep. 2010.
[25] M. Dini, A. Romani, M. Filippi, and M. Tartagni, "A nanocurrent power management IC for low-voltage energy harvesting sources," *IEEE Trans. Power Electron.*, vol. 31, no. 6, pp. 4292–4304, Jun. 2016.
[26] E. Dallago, A. L. Barnabei, A. Liberale, G. Torelli, and G. Venchi, "A 300-mv low-power management system for energy harvesting applications," *IEEE Trans. Power Electron.*, vol. 31, no. 3, pp. 2273–2281, Mar. 2016.
[27] L. Wu, X. D. Do, S. G. Lee, and D. S. Ha, "A self-powered and optimal SSHI circuit integrated with an active rectifier for piezoelectric energy harvesting," *IEEE Trans. Circuits Syst. I, Reg. Papers*, vol. 64, no. 3, pp. 537–549, Mar. 2017.
[28] A. Romani, M. Filippi, and M. Tartagni, "Micropower design of a fully autonomous energy harvesting circuit for arrays of piezoelectric transducers," *IEEE Trans. Power Electron.*, vol. 29, no. 2, pp. 729–739, Feb. 2014.
[29] S. Priya and D. J. Inman, *Energy Harvesting Technologies*, vol. 21. Berlin, Germany: Springer-Verlag, 2009.
[30] A. E. Fitzgerald, C. Kingsley, and S. D. Umans, *Electric Machinery*, 6th ed. New York, NY, USA: McGraw-Hill, 2005.
[31] D. K. Cheng, *et al.*, *Field and Wave Electromagnetics*. Noida, India: Pearson Education India, 1989.
[32] B4201 Specification Sheet, (2017). [Online]. Available: www.kjmagnetics.com, Accessed on: Apr. 2017.
[33] CATALOG #8, (2011). [Online]. Available: www.piezo.com, Accessed on: Apr. 2017.
[34] A. Abasian and A. Tabesh, "A characterization method for identifying the piezoelectric bending beam energy harvesters," in *Proc. 2016 4th Int. Symp. Environ. Friendly Energies Appl.*, 2016, pp. 1–4.
[35] A. Tabesh and L. G. Frechette, "An improved small-deflection electromechanical model for piezoelectric bending beam actuators and energy harvesters," *J. Micromech. Microeng.*, vol. 18, no. 10, 2008, Art. no. 104009. [Online]. Available: http://stacks.iop.org/0960-1317/18/i=10/a=104009

Alireza Abasian (S'14) was born in Isfahan, Iran, in 1986. He received the B.Sc. degree in electrical engineering from the University of Tehran, Tehran, Iran, in 2009, and the M.Sc. degree in electrical engineering from Isfahan University of Technology (IUT), Isfahan, Iran, in 2012. He is currently working toward the Ph.D. degree in electrical engineering at the Department of Electrical and Computer Engineering, IUT.

He has been a Researcher with the Renewable Energies and Energy Harvesting Laboratory, IUT, since 2012. His research interests include energy harvesters, smart grids, renewable energy systems, switching power supplies, and power electronics and its applications.

Ahmadreza Tabesh (S'01–M'06) received the Ph.D. degree in electrical engineering (energy systems) from the University of Toronto, Toronto, ON, Canada, in 2005.

He was a Postdoctoral Fellow and Research Associate with the Center for Applied Power Electronics, University of Toronto (2005–2006) and the Microengineering Laboratory for MEMS, Department of Mechanical Engineering, University of Sherbrooke, Sherbrooke, QC, Canada (2006–2009). He is currently an Associate Professor with the Department of Electrical and Computer Engineering, Isfahan University of Technology, Isfahan, Iran. His research interests include grid integration of renewable energy resources, dc microgrids, and energy harvesters for powering smart monitoring devices.

Abolghasem Zeidaabadi Nezhad was born in Sirjan, Iran, in 1961. He received the B.Sc. degree in electronics engineering from Shahid Bahonar University of Kerman, Kerman, Iran, in 1988, and the M.Sc. and Ph.D. degrees in communication engineering from Sharif University of Technology, Tehran, Iran, in 1991 and 1997, respectively.

Since 1997, he has been with the Isfahan University of Technology, Isfahan, Iran, where he is currently an Associate Professor with the Department of Electrical and Computer Engineering. His areas of interest include electromagnetic field problems, antennas, and microwave engineering.

Nasrin Rezaei-Hosseinabadi (S'14–M'17) was born in Isfahan, Iran, in 1986. She received the B.Sc., M.Sc., and Ph.D. degrees all in electrical engineering from Isfahan University of Technology (IUT), Isfahan, Iran, in 2008, 2010, and 2016, respectively.

She is currently an Assistant Professor with the Department of Electrical and Computer Engineering, University of Technology, Isfahan, Iran. Her research interests include low power on-chip converters for portable electronic devices and energy harvesting system design.